An Orientationally Ordered Hierarchical Exfoliated Clay−Block Copolymer Nanocomposite

Yung-Hoon Ha,[†] Younghwan Kwon,[⊥,‡] Thomas Breiner,[†] Edwin P. Chan,[†] Theodora Tzianetopoulou,[§] Robert E. Cohen,[‡] Mary C. Boyce,[§] and Edwin L. Thomas*[,†]

Department of Materials Science and Engineering, Department of Chemical Engineering, and Department of Mechanical Engineering, Massachusetts Institute of Technology, Cambridge, Massachusetts 02139

Received November 11, 2004; Revised Manuscript Received April 6, 2005

ABSTRACT: Creation of an orientationally ordered hierarchical nanocomposite can be done by the preferential insertion of individual polymer-covered clay layers into block copolymer (BCP) microdomains—in the present instance, PS-functionalized silicate layers into the polystyrene (PS) domains of a styrene−butadiene−styrene triblock copolymer (SBS). We present here the method required to achieve such an ordered block copolymer−nanoparticle composite and report preliminary mechanical properties. PS is grafted-to or polymerized-from individual clay sheets in order to provide a neutral enthalpic interaction between the PS chains on the clay layers and the PS blocks in the SBS. The molecular weight of the PS chains tethered to the clay was varied, and we show that higher molecular weight is critical in obtaining individual clay sheets dispersed in the SBS matrix. When exfoliated, the clay sheets serve as a template for the lamellar domains. Because of their large areal dimensions and concentration, the clay particles likely form a discotic nematic that is responsible for the observed orientational flipping transition of the BCP layers during the roll-cast process. We also show through experiments and simulations that the mechanical properties of these anisotropic hierarchical nanocomposites are not significantly changed by the insertion of 2 wt % of the clay sheets for deformation parallel to the lamellae.

Introduction

Many researchers have pursued nanocomposites based on either intercalated or exfoliated clay dispersed into various matrix polymers.[1−8] However, to date, there has not been a report of an exfoliated nanocomposite structure within a block copolymer matrix.[9−16] Forming an exfoliated clay nanocomposite is a challenge due to the unfavorable interactions between the intrinsically hydrophilic clay and the hydrophobic matrix polymer chains.[17−21] Thus, methods of organically functionalizing the surfaces of the clay, utilizing the inherent negative surface charges on the clay layers, have been successfully developed.[22,23]

The underlying thermodynamic factors for intercalation of organically functionalized layered-silicates were first examined by Vaia et al.[17,18] using a mean field statistical lattice model for melt intercalation. In particular, they considered the case of an organically modified layered-silicate dispersed in an amorphous homopolymer matrix. Their analysis concentrated on clays with ion-exchanged short alkylammonium surfactants that are typical of commercial samples and demonstrated that the conformational entropy gained by the surfactant in the now thicker clay galleries effectively offsets the loss of the conformational entropy of the homopolymer chains that enter into the slitlike regions between clay layers. Moreover, since the enthalpic interaction between the alkyl portion of the surfactant chains and the clay surface is strongly repulsive, if polymers possessing Lewis acid/base groups are utilized, favorable interactions will arise between these electron donating/accepting groups on the polymer backbone and the silicate layers. As the polymer and the surfactant interactions are repulsive, portions of the polymer chain absorb onto the clay surface, leading to intercalation. Comparison of these theoretical predictions to experimental systems shows remarkable agreement.[18]

Recently, Balazs et al.[19,20] used a numerical self-consistent-field theory to further elucidate the thermodynamics of intercalation vs exfoliation. In their approach, all enthalpic interactions are treated through various Flory−Huggins parameters, and the authors focus on the effect of the molecular weight of the surfactant. In the cases where intercalation or exfoliation is observed, the free energy decreases with increase in the clay sheet separation distance and reaches a plateau value. Balazs et al. treat the case for a favorable polymer−clay surface interaction and observe similar results to Vaia et al. where intercalation is preferred. Except for this special case, the simulations set both the enthalpic interactions (χ) between the layered-silicate surface and the matrix polymer pair and the layered-silicate surface and the surfactant chain pair to be neutral ($\chi = 0$). For the case of neutral enthalpic interactions between the matrix polymer and the surfactant chains, increased surfactant molecular weights favor intercalation due to the larger gain in conformational entropy of the surfactant with increasing clay layer separation. Furthermore, the authors find there is an optimum surfactant grafting density, as at one extreme, densely packed surfactant chains do not allow the polymer chains to intermix and at the other extreme, a nearly bare silicate surface will provide es-

[†] Department of Materials Science and Engineering.
[‡] Department of Chemical Engineering.
[§] Department of Mechanical Engineering.
[⊥] Present address: Department of Chemical Engineering, Daegu Univeristy, Gyeongsan, Gyeongbuk 712-714.
* To whom correspondences should be addressed: e-mail elt@mit.edu.

10.1021/ma0476792 CCC: $30.25
Published on Web 05/18/2005

sentially no mixing entropy contributions for the surfactant with the polymer. As expected, intercalation/exfoliation is favored when $\chi < 0$ whereas $\chi > 0$ leads to immiscible systems.

To investigate the theoretical predictions, Beyer et al.[24] synthesized polystyrene (PS)-functionalized montmorillonites of varying molecular weights (through the traditional cation exchange technique using quaternary amine-terminated PS surfactants) and studied the melt blended PS-grafted-clay/homopolystyrene composites using small X-ray scattering (SAXS) and transmission electron microscopy (TEM). For 5 wt % (inorganic content) PS-functionalized montmorillonite added into a PS matrix of 10 000 g/mol (replicating $\chi = 0$) they observe via SAXS and TEM an immiscible blend for all PS surfactant molecular weights explored ($M_n = 1700-17\,000$ g/mol). They argue that the immiscibility could result from an excessive grafting density, from an autophobic dewetting as observed in colloidal systems,[25] or from too small a difference in the enthalpic interactions between the clay surface and the surfactant vs the clay surface and the polymer chain, as discussed previously by Vaia.[17] Laus et al.[9] also refer to an unpublished report from their laboratory where the use of longer (18 repeat units) alkyl surfactants led to intercalation of the SBS chains (note in this case the homopolymer matrix is a block copolymer) whereas shorter (10 repeat units) alkyl surfactants led to immiscible behavior in a clay−SBS system.

Utilization of a BCP as the matrix in clay nanocomposites raises several interesting questions. The creation of a clay−block copolymer (C−BCP) nanocomposite with the clay as single exfoliated sheets presents a potentially interesting material since the size and shape of the BCP microdomains are readily controlled by choice of BCP composition and molecular weight while the microdomain orientation can be controlled by various types of fields applied during processing. Previously, we attempted to create a C−BCP nanocomposite via solution roll-casting of a Cloisite 10A layered silicate with an SIS lamellar triblock and found that this processing approach only produced intercalated clay particles in the SIS matrix rather than a nanocomposite of exfoliated clay sheets within the SIS.[16] A review on clay−block copolymer nanocomposites up to 2002 is provided in this reference.[16] Since then, Hasegawa and Usuki examined a clay−SEBS triblock system and showed that the SEBS domains are templated around the intercalated clay particles after melt compounding.[26] Lee et al.[27] studied a SIS with a montmorillonite clay and found an intercalated structure that adversely influenced the alignment of the PS cylinders during large-amplitude oscillatory shear. Thus, the ideal globally oriented, single silicate sheet within a lamellar microdomain hierarchical nanocomposite remains unattained. Theoretically such a system is indeed possible. As opposed to homopolymer matrices, BCP matrices can be considered as mesophases with long-range elastic forces due to the periodic microphase separation in the material. Groenewold and Fredrickson[21] investigated the effect of the elastic stresses on the stability of a lamellar nanocomposite when clay layers are inserted into the block copolymer matrix. The enthalpic/entropic miscibility criterion, as outlined by the Vaia and the Balazs theories, was assumed satisfied, and the energetic penalties associated with the deformation of the BCP lamellar domains with the insertion of a clay layer were calculated to generate stability maps. In the case of clay layers possessing more rigidity than the BCP matrix polymer chains (the most realistic scenario), the elastic energetic penalties are not significant and the exfoliated state is stable.

There are many additional variables introduced through the use of BCP as the matrix material that can determine whether intercalation or exfoliation takes place. Namely, composition of the blocks, molecular weight of each block, chain architecture of the BCP (e.g., diblock vs triblock vs star diblock, etc.), solvent, the processing temperature, the order−disorder transition temperature, and the overall polymer concentration all require consideration. The presence of two different types of monomeric units in the polymer chain necessitates treating the different enthalpic interactions of the clay with each block. Moreover, to allow geometrical compatibility between the layered-silicate and the microdomains of the BCP (assuming no particle-induced BCP morphology transformation), the functionalized clay needs to be attracted into the majority component phase of the BCP. For example, in spherical and cylindrical microdomains, the clay can only be accommodated in the majority phase whereas a lamellar morphology may accommodate clay layers in both the majority and minority phases. Note that in a double-gyroid morphology the insertion of individual clay layers in either type of domain would be energetically costly. Additionally, the molecular weights of the blocks not only affect the entropic interactions between the clay surfactants and the BCP as discussed above but also affect the order−disorder transition temperature of the BCP. For commercially important styrene−dienic block copolymers with typical total molecular weights of 50 000−100 000 g/mol, the order−disorder temperature of the BCP is well above the degradation temperature. Thus far, high-temperature melt blending, while promoting intercalation, has not led to an exfoliated clay−BCP system.

In the present study, a fully exfoliated C−BCP structure was obtained via a two-step procedure. First, PS chains were attached to the clay surface either by grafting-to end-functionalized PS molecules or polymerizing from the clay surface to form tethered PS chains. Then the PS covered clay sheets were solution-blended with a SBS triblock and the roll-cast to form oriented C−BCP films. Lower molecular weight PS (∼1−2 kg/mol) covered sheets produced C−BCP samples with an intercalated structure. Exfoliated structures were obtained using clays functionalized with ∼6−7 kg/mol PS chains. In the 6 kg/mol C−BCP nanocomposite, the clay nanoparticles were well oriented in-plane which leads to a reorientation of the BCP layers from the perpendicular to the parallel orientation during roll-casting. Finally, we note that at these low (2 wt % clay) loadings the orientationally ordered exfoliated C−BCP nanocomposite does not exhibit any modulus and yield strength enhancements over the neat BCP when deformed parallel to the lamellae.

Experimental Section

I. Materials. The layered-silicate employed was a natural sodium montmorillonite (Southern Clay Products Cloisite Na^+) that was chemically modified to tether a PS shell around the inorganic layer. Clays modified through surface-initiated polymerization ("grafting-from") following the synthesis scheme of Weimer et al.[28] are denoted as FC (from-clay), and samples modified through cation exchange reaction ("grafting-to") are

Table 1. Molecular Weight and Polydispersity Index for the Four Classes of PS Chains Tethered on Montmorillonite[a]

	number-average mol wt (g/mol)	PDI	theor wt % of PS	measd wt % of PS	relative grafting density (%)	XRD spacing (nm)
neat clay						1.0
1K TC	1400	1.12	58	60	103	5.0
7K TC	7100	1.04	88	66	75	11.0
1K FC	900	1.48	45	43	96	4.2
6K FC	6000	1.26	83	80	96	12.6

[a] TC represents PS chains grafted *to clay,* and FC represents PS synthesized *from clay*. The grafting density is estimated by taking the ratio of the measured amount of organic content relative to the theoretical amount it should possess at the molecular weights measured and CEC reported (95 mequiv/100 g). The layer spacing of the PS modified layered-silicates is also reported.

denoted as TC (to-clay). The amino-functionalized PS was prepared according to the scheme provided by Ueda et al.,[29] and the cation exchange was carried out as described by Hoffmann et al.[30] (95 mequiv/100 g). The molecular weight (as determined by GPC) and the polydispersity index (PDI) of the PS grafts (cleaved from clay surface for TC samples by refluxing with LiBr in THF) are shown in Table 1.

The SBS triblock used was the commercially available Vector 4461-D. The molecular weight of each of the polystyrene end blocks was 18 500 g/mol, and that of the polybutadiene midblock was 45 000 g/mol (PDI = 1.03[31]). The composition is 45 wt % styrene, and the pure triblock microphase separates into a lamellar structure with PS and PB domains approximately 12 and 14 nm thick, respectively, giving a lamellar repeat spacing of 26 nm.[32] The mechanical properties of roll-cast Vector 4461-D have been extensively studied.[32]

II. Sample Preparation. Prior to blending the PS covered clay sheets with the triblock copolymer, excess untethered PS was extracted through a preferential solubility method. For each PS molecular weight, untethered PS was dissolved in 5% THF solution, and then methanol (a nonsolvent) was added dropwise until cloudiness appeared, indicating the precipitation of PS. This was taken as the upper bound of the amount of methanol required for untethered PS precipitation. A 5 wt % THF solution was then prepared from PS tethered clay, and methanol was added dropwise again. This will precipitate out the PS-functionalized clay first since the grafting of PS to clay effectively creates a much larger molecular weight species. As expected, the point at which cloudiness appeared was much lower than that for the free PS. The precipitates were then centrifuged and collected; the supernatant containing the unbound PS was discarded. This process was repeated three times to ensure minimal free PS in the sample.

Tethered PS clay and SBS were then separately dissolved in 90/10 THF/cumene mixtures at approximately 2 wt % so that the combined solutions would result in a 2 wt % inorganic content clay/SBS nanocomposite in the final solvent-free state. (This solvent mixture was utilized to slow down the evaporation of the solvent during the latter stages of the roll-casting process since previous experiences in our laboratory indicated that the late stage of roll-casting where the viscous solution transfers onto the metal roller is key for good alignment.) The solvent was allowed to evaporate while the sample was on top of a vibrator to prevent potential sedimentation of the clay until a honeylike viscosity was reached (approximately 40 wt % solution). The solution was then roll-cast, dried, and annealed as described previously.[33,34]

III. Thermogravimetric Analysis. To determine the amount of PS tethered to the clay, thermogravimetric analysis (TGA) was performed utilizing a Perkin-Elmer TGA7 under argon at a heating rate of 20 °C/min from ambient conditions to 900 °C. Samples were dried in a vacuum oven and kept at 70 °C for a few days prior to measurement to ensure complete removal of excess moisture and solvent.

IV. Morphological Characterization. The procedures used for XRD and TEM characterization have been reported previously.[16] The small-angle X-ray scattering (SAXS) studies were mostly carried out in the D1 beamline at the Cornell High Energy Synchrotron Source (CHESS). The beamline employs a 2D charge coupled detector (CCD) (1024 × 1024 pixels at 51 μm/pixel resolution), and the sample-to-detector distance was set at 980 mm with a wavelength of 0.155 nm. A Siemens SAXS machine consisting of a rotating anode X-ray source (Cu Kα, 0.154 nm) operating at 40 kV and 30 mA was also employed. A 2D CCD detector (512 × 512 pixels) was utilized with a sample-to-detector distance of 640 mm. SAXS data interpretation was performed using a freely downloadable software, Fit2D, which allows a host of powerful data extraction tools.[35,36]

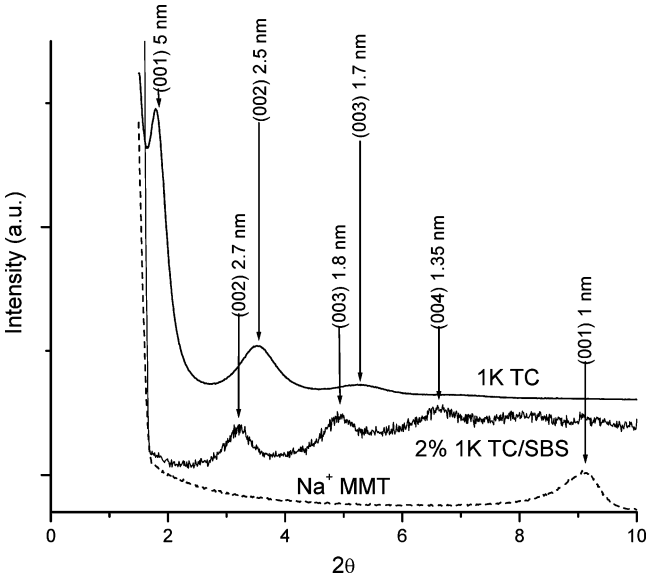

Figure 1. XRD patterns of natural sodium montmorillonite, montmorillonite exchanged with 1400 g/mol amino-terminated polystyrene (1K TC), and 2 wt % 1K TC−BCP. Note the spacing increase from approximately 1 to 5 nm after functionalization of the clay and subsequent intercalation when incorporated with SBS. The intensities have been vertically shifted by an arbitrary amount.

Results

I. Characterization of the PS-Modified Layered-Silicates. After tethering PS onto clay, extraction of the free PS and sample drying, XRD and TGA analyses were carried out. The XRD data in Figure 1 illustrate the influence of the "grafting-to" process on the clay. The layered-silicate spacing increases from ~1 nm (natural sodium montmorillonite (MMT)) to 5 nm (1K TC). XRD data for the 7K TC samples are omitted to clarify the plot, but patterns show the (003), (004), and (005) peaks, yielding a (001) spacing of 11 nm. The XRD data in Figure 2 illustrate the "grafting-from" process. The TEMPO initiator increases the layer spacing to 2.2 nm. After subsequent polymerization of a 6000 g/mol molecular weight PS, the 6K FC layer spacing is 12.6 nm. The data for the 1K FC modified clay are omitted for figure clarity, but XRD shows a layer spacing of 4.2 nm (see Table 1).

TGA analyses were performed to calculate the percentage of organic content after final purification of the PS tethered clay particles. By comparing the measured

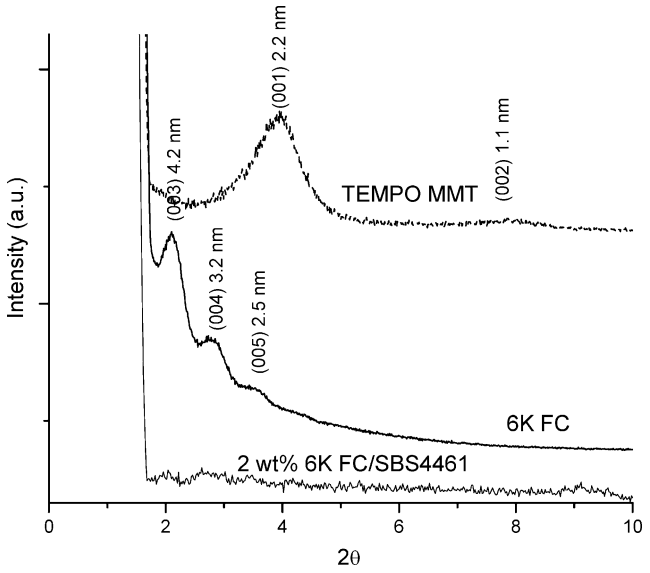

Figure 2. XRD patterns of the TEMPO initiator grafted onto natural sodium montmorillonite that shows an increased layer spacing (2.2 nm) over that of the natural clay spacing. Subsequent living free radical polymerization of PS to 6000 g/mol molecular weight results in a further increase in the layer spacing to 12.6 nm, which can be deduced from the (003), (004), and (005) peaks. Subsequent incorporation of the 2 wt % 6K FC into SBS resulted in no observable Bragg scattering in this regime, suggesting nearly complete exfoliation of the PS-modified clay.

organic content relative to the theoretical organic content calculated based on the PS molecular weights and the cation-exchange capacity (95 mequiv/100 g), the percentage of tethered sites relative to the total allowable sites can be calculated (the "relative grafting density"), and these results are also tabulated in Table 1. These results show that the layer spacing of the higher molecular weight 7K TC is somewhat *lower* than the 6K FC. This can be attributed to a lower grafting density with increasing molecular weight in the grafted to (TC) samples, resulting in a lower degree of chain stretching for the 7K PS grafts compared to the 6K PS grafts.

II. Characterization of the C−BCP Morphology. The morphology of oriented C−BCP films was studied using a combination of XRD, SAXS, and TEM along various roll-cast directions. Recall that $\hat{x}$ is the flow direction, $\hat{y}$ is perpendicular to the rollers (thickness direction), and $\hat{z}$ is the neutral axis (see Figure 3a). We confirmed the neat lamellar triblock copolymer morphology after roll-casting is the usual perpendicular orientation as shown in Figure 3b (layer normals along $\hat{z}$).[30] Figure 3c shows the orientation of the sample in the XRD experiments.

a. Grafting-to-Clay (TC) Samples. The TC−BCP composites, employing the clay with amino-terminated PS chains grafted onto the layered-silicate surface, are discussed first. Figure 1 shows the XRD pattern for the 2 wt % 1K TC−BCP. Note that the clay layer spacing increased to 5.4 nm after roll-casting, suggesting intercalation. Parts a and b of Figure 4 show the SAXS patterns taken with the incident beam along $\hat{x}$ and along $\hat{y}$, respectively, for the 2 wt % 1K TC−BCP. The (001) arcs show that this sample exhibits the usual preferred perpendicular orientation of the BCP[32] with the lamellar normals along $\hat{z}$, as schematically illustrated in Figure 4c. The TEM image in Figure 4d viewed along $\hat{x}$

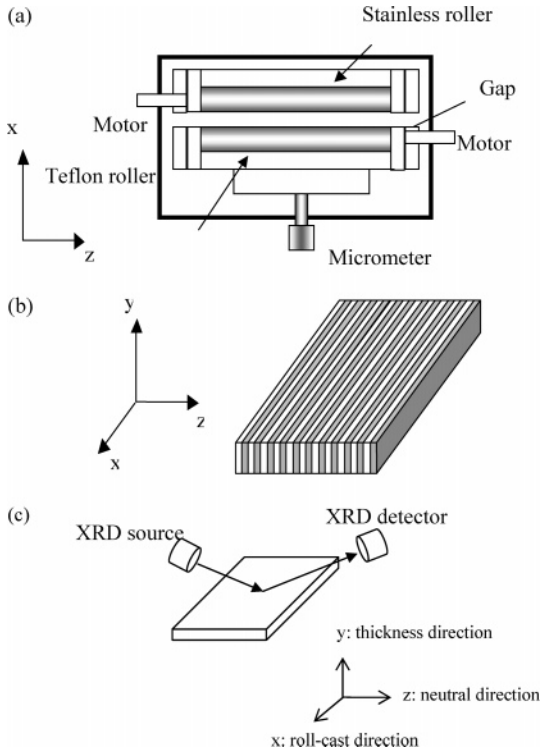

Figure 3. (a) Schematic representation of the roll-caster and the convention used to label the coordinate axes. (b) Roll-casting orients the lamellar triblock in the perpendicular state (lamellar normals pointed along $\hat{z}$). (c) Orientation of the roll-cast samples during XRD analysis.

confirms the perpendicular lamellar orientation and, in addition, shows thick, white regions suggestive of clay inclusions. When these regions are examined at higher magnification (see inset), the images show these regions are stacks of the PS grafted clay layers within a PS domain. Interestingly, TEM shows the normals of the oriented layered-silicate stack are on average *orthogonal* to the BCP lamellar normals. Typically there are approximately 5−20 layers of clay bundled together in a particular large white region. For example, the thickness of the white region in Figure 4d is approximately 50 nm, and the image shows nine adjacent clay layers. Thus, the average clay layer spacing is approximately 5.5 nm. Knowing the global orientation of the clay allows XRD, with the incident and reflected beam bisecting the *y*-axis, to more precisely probe the clay layer spacing. The X-ray results confirm the value deduced from the TEM image giving a clay layer spacing of 5.4 nm (compared to 5 nm for the original 1K TC stacks). Although the microdomains of the BCP are principally in the perpendicular orientation, TEM shows that in the periphery of the clay bundles many BCP domains locally arrange to maximize the PS layer contact around the clay bundles, creating packing defects in the lamellar order. Thus, the 1K TC−BCP sample exhibits a perpendicular orientation of the BCP with a parallel orientation of PS grafted clay stacks. This result is consistent with the morphology observed by us in another purely intercalated C−BCP system made by solution roll-casting clay particles and a similar triblock.[17]

Use of a higher molecular weight PS graft was also explored. SAXS patterns taken with the incident beam along the various directions of the 2 wt % 7K TC−BCP roll-cast sample predominantly exhibit a circular ring indicative of unoriented polycrystalline grains. TEM of

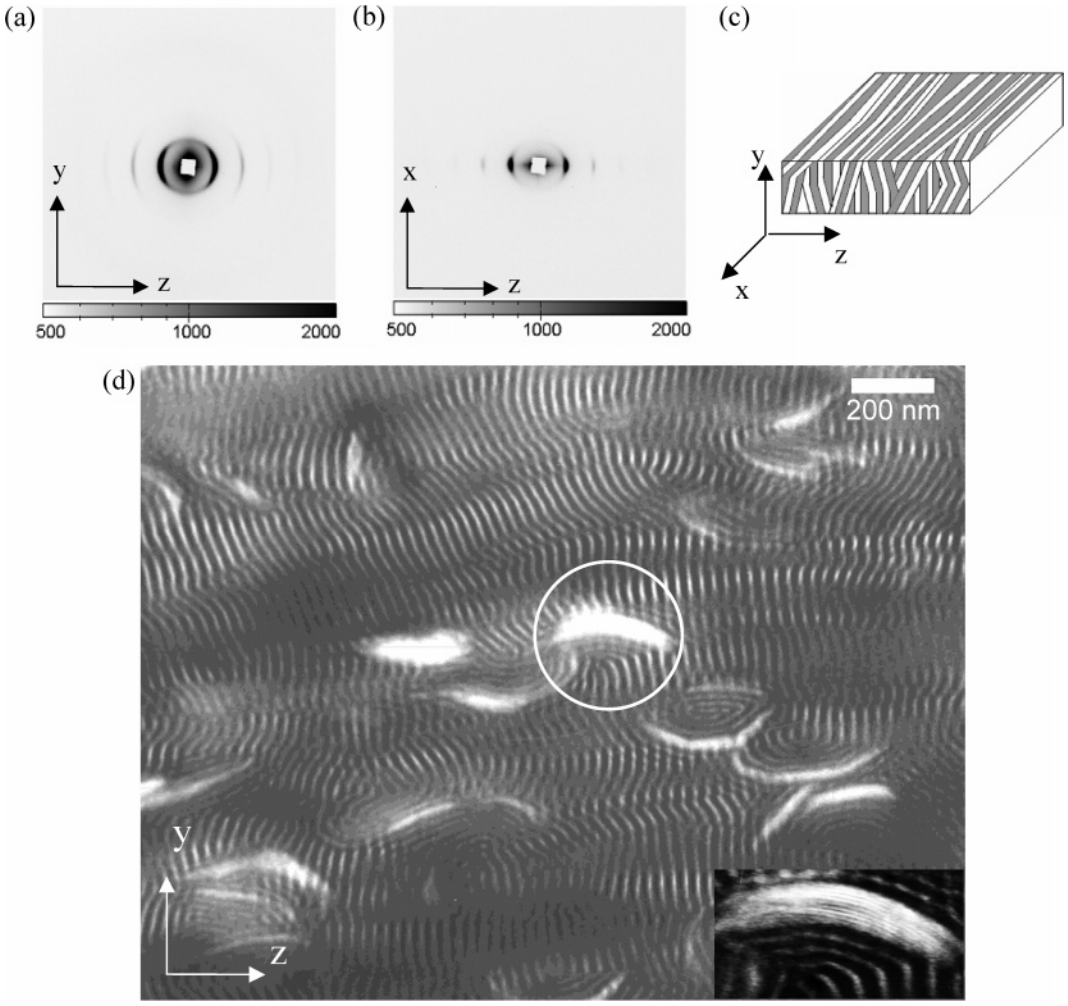

Figure 4. SAXS patterns taken of 2 wt % 1K TC−BCP with the incident beam along (a) $\hat{x}$ and (b) along $\hat{y}$. The BCP lamellae are oriented in a perpendicular orientation as shown in (c). (d) TEM of the nanocomposite viewed along $\hat{x}$ showing layered-silicates oriented orthogonally to the BCP lamellae. PS layers appear light due to OsO_4 staining of the PB layers. The high-magnification inset shows finely spaced black and white fringes indicative of the intercalated nature of the layered-silicates embedded in the PS domains.

microtomed sections shows grains in different orientations, in agreement with the SAXS results. The 7K TC PS-modified layered-silicates are again evident as white regions (e.g., circled regions in Figure 5), although each white region is generally considerably thinner than those in the 1K TC samples. TEM images exhibit a larger number of these white areas; on average, they are closer to one another, and there is a tendency for the white regions to be locally *parallel* to the microdomain layers. Scrutiny of high-magnification images of the individual white areas shows that typically there are only about 1−3 clay layers within a given white area. One other noticeable feature is the rather curved shape of many of the layered-silicates and the conformal nature of the adjacent BCP layers, leading to many defects and an overall lower degree of lamellar spatial order (in agreement with the absence of any higher order (00*l*) SAXS reflections) as well the lack of significant orientational order compared to the neat BCP material. Thus, the use of a higher molecular weight graft on the clay layers has produced a more exfoliated C−BCP nanocomposite but without global orientation.

b. Grating-From (FC) Samples. The FC−BCP composites employing the clay with surface initiated styrene polymerization are discussed next. SAXS data, with the incident beam along $\hat{x}$ and along $\hat{y}$ in parts a and b of Figure 6, respectively, show that roll-casting of the 2 wt % 1K FC−BCP once again leads to the perpendicular BCP orientation where the lamellar normals are aligned along $\hat{z}$. The TEM images are omitted for brevity but show thick white regions similar to Figure 4. Thus, C−BCP samples having 1K PS behave similarly regardless of the grafting process employed. Both the FC and TC clays form aggregated stacks when solution blended and roll-cast with the SBS triblock.

In the 2 wt % 6K FC−BCP sample, XRD data (Figure 2) do not show any discernible peaks, suggesting exfoliation of the clay particles. SAXS data viewed along $\hat{x}$ and along $\hat{y}$ in parts a and b of Figure 7, respectively, clearly demonstrate a well-aligned *parallel* orientation of the BCP (see Figure 7c). The full width at half-maximum (fwhm) $\Delta\mu_{yz}$ of the (001) peak is approximately 20°. Also note the absence of any higher order SAXS peaks. A highly aligned parallel orientation of the BCP layers should not lead to any Bragg scattering when the incident X-ray beam is along $\hat{y}$ as indeed confirmed in Figure 7b. The TEM image in Figure 7d viewed along $\hat{x}$ also confirms the well-aligned lamellae in the parallel orientation. The numerous thin, elongated white regions in the parallel orientation are single clay sheets. TEM shows each thickened PS domain contains a single dark line representing the edge-on

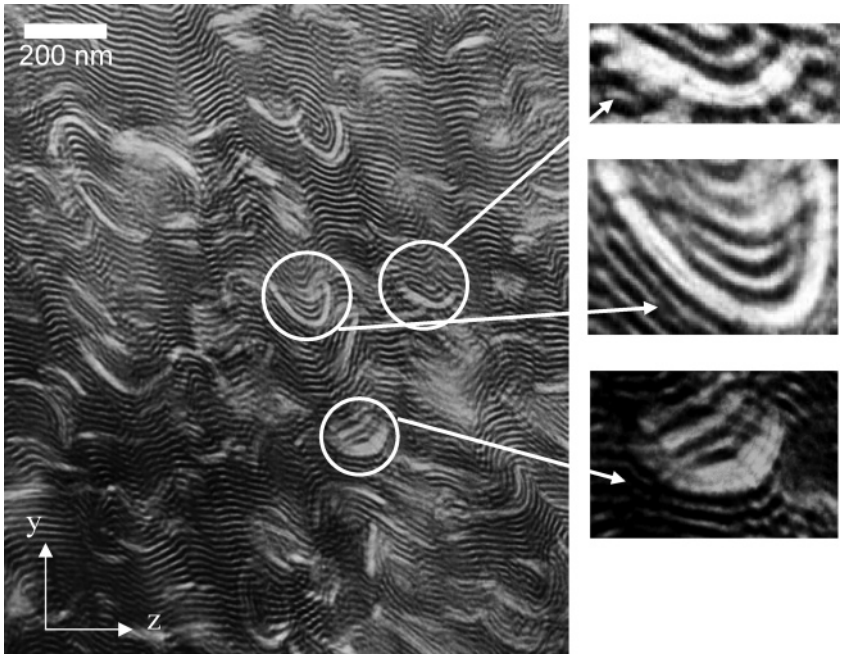

Figure 5. TEM viewed along $\hat{x}$ of the 7K TC−BCP nanocomposite showing layered-silicates oriented parallel to the BCP lamellae. Magnified regions showing PS domains containing 1 (top, middle) or 3 (bottom) silicate layers.

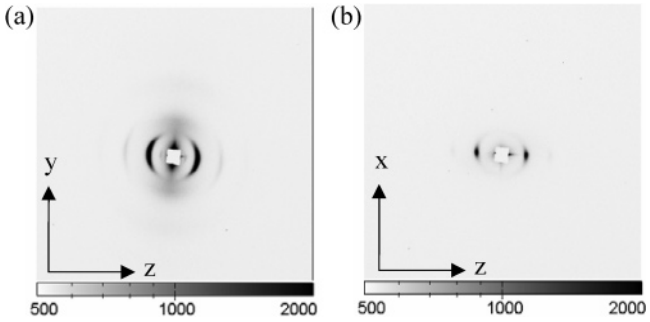

Figure 6. SAXS patterns of 2 wt % 1K FC−BCP with the incident beam along (a) $\hat{x}$ and (b) $\hat{y}$. The BCP lamellae are oriented in a perpendicular orientation similar to the 1K TC−BCP sample.

view of a clay sheet (see Figure 7e). This interpretation can be quantitatively checked. Since the neat BCP PS domains are approximately 12 nm thick, and the layer spacing of the pure 6K FC clay was measured to be 12.6 nm, the approximately 2× increased layer thickness observed in the TEM verifies that the thicker white domains contain only 1 clay sheet (see schematic Figure 7f). The fast Fourier transform power spectrum of the TEM image is very similar to the SAXS pattern (see inset to Figure 7d). In both patterns, only a single (001) reflection is observed due to the disruption of the long-range BCP lamellar order along the lamellar normal by the erratic yet frequent insertion of individual clay sheets, each creating a 2× thicker PS domain. XRD studies, with the incident and reflected beams bisecting $\hat{x}$, as shown in Figure 2, yield no noticeable scattering peaks over the q range probed, indicating the absence of stacks of PS grafted layers in the BCP matrix.

In this highly exfoliated sample, the much more numerous single clay layers induce a *flipping transition* during roll-casting of the BCP domains from the usual perpendicular orientation that occurs in the neat BCP and in the other PS functionalized clay−BCP composites. The lamellar flipping transition in the 6K FC−BCP exfoliated nanocomposite can be understood as follows: The energetically favored state of the layered-silicate appears to be in-plane (parallel orientation) for the layered-silicate nanocomposites whether compression-molded, simple-cast, or roll-cast.[4,37−40] Thus, in the early stages of roll-casting, the flow field guides the clay layers to lie in the parallel orientation and the grafted PS chains sterically stabilize the clay sheets, resembling a globally oriented lyotropic discotic nematic state. After further solvent evaporation, the BCP undergoes microphase separation, and the BCP lamellae nucleate around the numerous PS-functionalized sheets directing the global orientation of the BCP into the parallel orientation.

III. Mechanical Properties. a. Experimental Results. Because of the shape of the roll-cast films, only the in-plane mechanical properties can be readily assessed. Of the various composites produced, the one with the most idealized morphology, namely the globally oriented 6K FC−BCP nanocomposite with the single, nearly flat, clay sheets and BCP layers in parallel orientation, was subjected to uniaxial tension with the applied force on average parallel to the polymer layers and the clay sheets (i.e., force along $\hat{x}$ or $\hat{y}$). Figure 8 shows the C−BCP stress−strain curve overlaid on the corresponding (in this case $\hat{x}$ direction loading) data from that of a roll-cast neat SBS sample containing the perpendicular morphology[32] deformed along $\hat{x}$ (parallel to the layers). Surprisingly, the modulus (120 MPa) of the C−BCP is 30% lower than the neat BCP (180 MPa),[32] and the yield (or rollover) stress of the C−BCP is approximately 20% lower, indicating a somewhat *detrimental* effect of the exfoliated clay on the properties of the nanocomposite. A beneficial effect of the clay on the stress−strain behavior occurs in the large strain postyield region, where the onset of strain hardening is found to occur at considerably lower strains and the rate of strain hardening is higher compared to the neat BCP.

b. Micromechanical Simulation Results. Finite element based micromechanical simulations were carried out on representative volume elements (RVEs) of

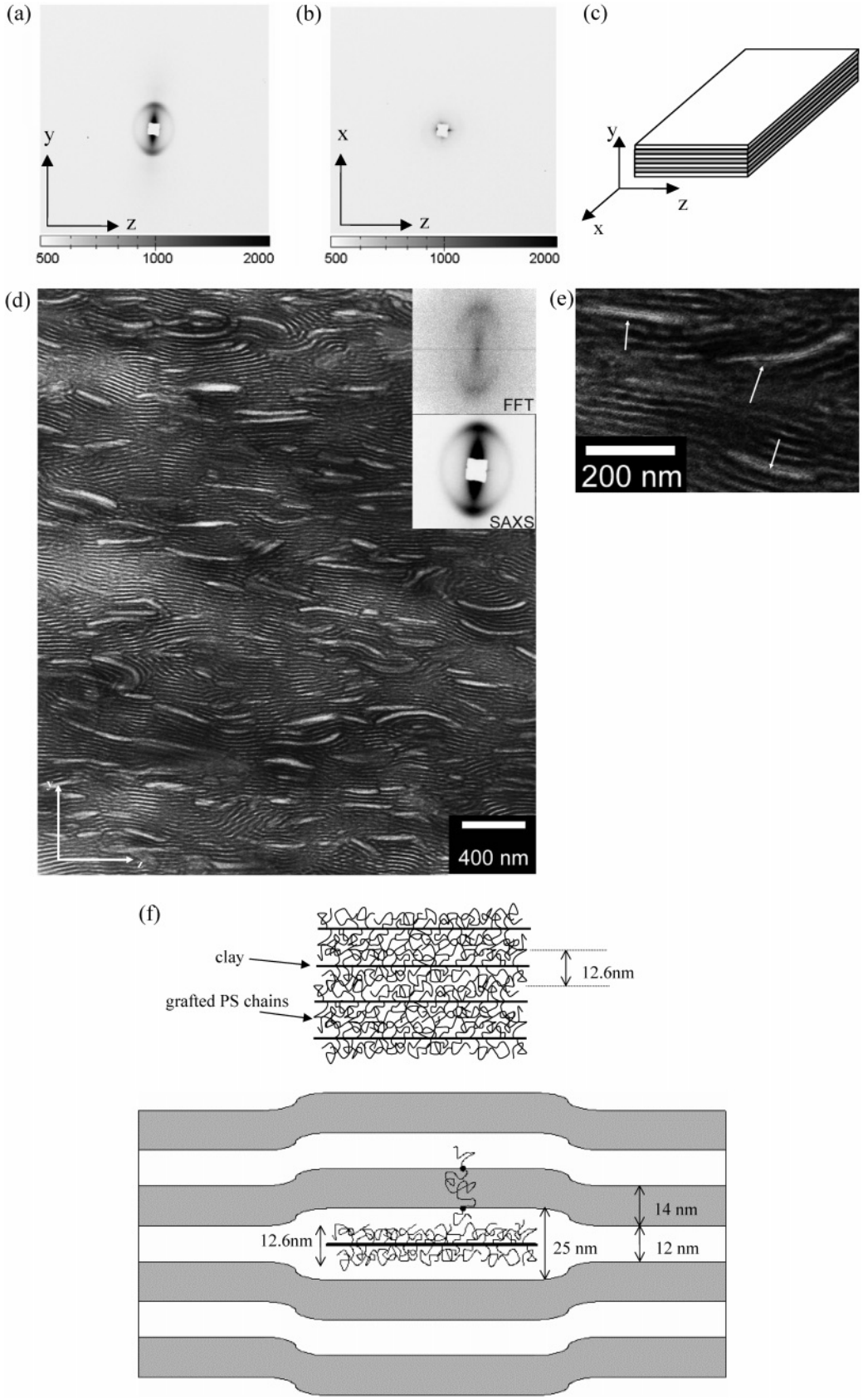

Figure 7. SAXS patterns taken of 2 wt % 6K FC−BCP with the incident beam along (a) $\hat{x}$ and (b) along $\hat{y}$. The BCP lamellae are now oriented in a *parallel* orientation as shown schematically in (c). Note there is little or no Bragg scattering in (b). (d) TEM image viewed along $\hat{x}$ of the nanocomposite showing layered-silicates oriented parallel to the BCP lamellae. Note the similarity between the FFT of the TEM image and the SAXS pattern. (e) This high-magnification image shows the exfoliated nature of the layered-silicates, shown as single dark lines, surrounded by the thicker PS domains. (f) Schematic illustration of the preferential local layer thickening observed in the PS domains. As measured from XRD, the layer spacing is 12.6 nm when the 6K FC sheets are stacked together. The thickness of the PS domain containing a clay layer will increase to $12 + n12.6$ nm, where n is the number of clay layers.

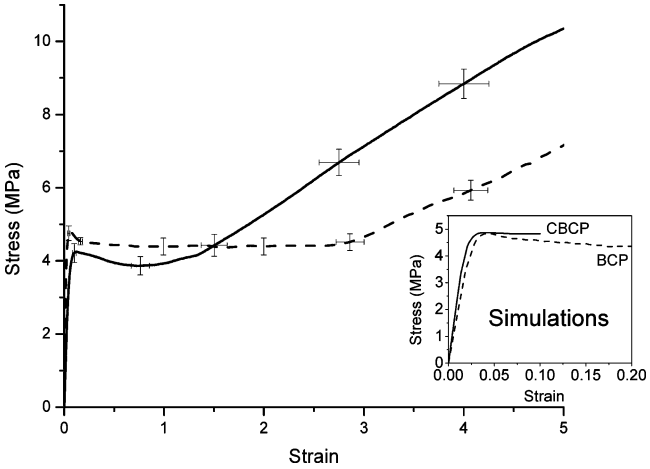

Figure 8. Stress−strain curves of the exfoliated 6K TC−BCP clay block copolymer nanocomposite and the neat SBS previously studied by Cohen et al.[32] The applied force is parallel to the layers. The C−BCP displays a lower modulus (120 MPa) as compared to the neat triblock (180 MPa), due primarily to the lower orientation of the BCP lamellae in the composite material. The onset of strain hardening occurs at significantly lower strains for the C−BCP nanocomposite. The overlaid error bars represent the maximum/minimum variations of the stress and strain values from five different samples from which the average stress−strain curve is plotted. The inset shows the stress−strain curves based on finite element calculations. At this level of clay loading (2 wt %), modeling predicts a very modest improvement in modulus and yield stress even in the ideal scenario where all lamellar domains and clay particles are perfectly aligned parallel to the force direction.

the neat BCP and the exfoliated C−BCP nanocomposite. The images shown in Figure 9 represent the resulting contour plots of the Mises equivalent stress, where the stress levels increase from blue to red. The simulations represent parallel loading of an ideally oriented BCP structure and an ideally oriented C−BCP nanocomposite incorporating 2 wt % of exfoliated clay sheets. Sample orientation is assumed to be perfect, and the individual clay sheets are assumed flat and of zero effective thickness so as to not swell the PS domains and disrupt the orientation. This scenario allows the determination of the upper bound of the parallel stiffness of the BCP and C−BCP materials at a clay loading of 2 wt %.

The response of the neat BCP to loading parallel to the lamellar orientation is dominated by the behavior of the glassy PS layers (orange layers). As shown in Figure 9a ($\epsilon = 4.9\%$), micronecking initiates in individual PS layers. The micronecks follow the basic behavior observed in macroscopic necking of polymers where the neck initiates, localizes, then stabilizes, and propagates upon reaching the natural draw ratio of the material. Shear bands initiate on PS/PB interfaces at the sites of micronecks (see $\epsilon = 6.6\%$) and progress through the adjacent PB layer to the next PS/PB interface, causing another microneck to initiate in the neighboring PS layer at an approximate offset angle of 45°. This produces a periodic cascading of micronecks throughout the PS layers (see $\epsilon = 9.2\%$). The periodic cascade of deformation events is a mechanism for the propagation and spreading of deformation and damage that is also observed in other layered materials such as microlayered polymers.[41] With this deformation process, the micronecks multiply and, at a macroscopic level, form a neck. Once the micronecks have fully cascaded, each will locally draw along its respective layer, ultimately producing the observed macroscopic strain hardening and eventually internal PS domain fragmentation (see $\epsilon = 35.2\%$). Cohen et al.[32] experimentally observed similar stress−strain curves as well as the fragmentation within the PS layers of the macroscopically necked region of SBS during in-situ SAXS deformation studies. In our samples, macroscopic shear bands could easily be observed via cross-polarized light microscopy propagating just ahead of the necked regions. These macroscopic shear bands propagate on a different length scale by a mechanism similar to the microscopic shear bands.

Discussion

The mechanical property simulations of the C−BCP nanocomposite indicate that even in the ideal material, the insertion of clay sheets in the rigid PS domains leads to minimal enhancement in the modulus (see Figure 8, inset). The elliptical region in Figure 9c (see $\epsilon = 4.3\%$ in Figure 9b) is an enlargement of the C−BCP microstructure, depicting a single load carrying clay layer embedded at the center of a PS domain. Experimentally, however, the exfoliated clay sheets in the BCP decrease the overall degree of alignment of the lamellae (see Figure 7d) that results in a more compliant initial response (see Figure 8). In some regions, the BCP domains follow the curved shape of the exfoliated clay particles, causing greater layer misorientation and the creation of defects within the BCP structure. These effects lead to a fwhm (full width at half-maximum) azimuthal spread of the (001) SAXS reflection for the C−BCP of 20°, considerably higher than the typical 10° fwhm for the neat triblock. The greater spread in the layer orientation in the C−BCP material with respect to the loading direction leads to a strong modulus decrease since modulus varies with misorientation angle (ϕ) as $\sin^4 \phi$.[42,43]

The simulations also show that clay sheet boundaries are regions of stress concentration in the PS layers that act as the initiation sites for the micronecks (see $\epsilon = 6.6\%$). The "cascade" pattern of micronecks does not follow as regular a pattern as in the neat block copolymer material. Instead, micronecks cascade between particle edges. The particles "shield" a large surrounding region of both the PS and PB from deforming due to their much higher stiffness with respect to the two BCP constituents. Because of the "shielding" effect, the macroscopically applied strain must be accommodated by the remaining free-to-deform material that, as a result, must undergo greater local stretch at any given macroscopic strain than in the neat material. This mechanism nicely explains the onset of strain hardening at lower strains in the C−BCP compared to neat BCP and suggests that by controlling the clay aspect ratio and weight fraction the strain hardening and natural draw ratio of these materials could be tailored. The roll-cast, in-plane layer orientation of the film samples limits the deformation studies to a single direction of a highly anisotropic sample. Other directions of loading may lead to significantly differing behavior, and studies are currently underway to predict these behaviors through simulation.[44] The in-plane layering of the exfoliated clay and the BCP domains is highly favorable for permeability applications due to the large number of individual impermeable clay layers.

Conclusions

We have explored both grafting-to clay and grafting-from clay (TC and FC) approaches to create exfoliated

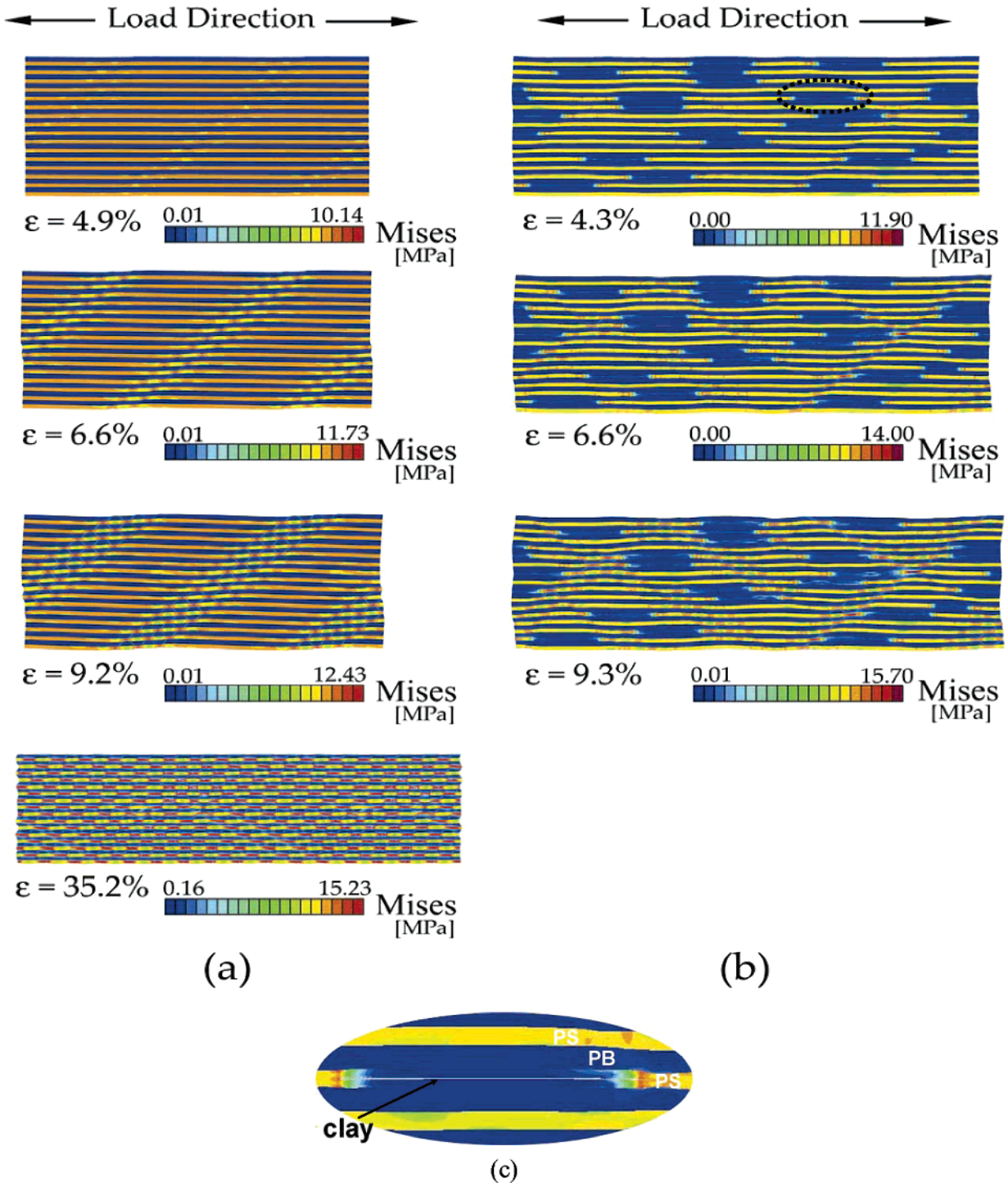

Figure 9. Contours of Mises equivalent stress at various levels of macroscopic strain in (a) the neat BCP material and (b) the C−BCP material. Both materials are observed to accommodate the macroscopic strain via localized micronecking within the PS layers. The micronecks cascade from PS layer to PS layer via shear banding of the PB layers. The clay particles interrupt microneck propagation and shield large regions of PS and PB layers from deforming. (c) Enlargement of the microstructure at a region containing a clay sheet. The single load carrying clay layer embedded at the center of a PS domain is surrounded by the lower stress (blue color) PS and PB layers. The edges of the clay layer create stress concentrations leading to PS breakup while the surrounding BCP layers are shielded from experiencing high strains. Properties used: E_{PS} = 386 MPa, ν_{PS} = 0.33, E_{PB} = 4.4 MPa, ν_{PB} = 0.487, E_{clay} = 170 GPa, and ν_{clay} = 0.22.

clay−block copolymer (C−BCP) hierarchical nanocomposites. A key factor for producing single clay layer block copolymer nanocomposite is to ensure that the polymer tethered to the clay surface is of sufficient molecular weight to sterically stabilize the clay sheets during the solution roll-casting process. In the case of the 6K and 7K PS graft samples, the higher molecular weight PS chains serve to stabilize the clay sheets, and as the relaxation times decrease, the system orders into a discotic-like nematic. Then as the disorder to order concentration is crossed, the numerous individual clay sheets now serve to nucleate in-plane (parallel) orientation of the triblock layers leading to the observed lamellar flipping transition. This appears to be the first experimental demonstration that dispersed nanoparticles can dictate the global orientation of a block

copolymer. Because of the increased BCP layer misorientation caused by the incorporation of the clay sheets into the lamellar BCP, the in-plane modulus and yield strength of the exfoliated C−BCP nanocomposite is lower than that of the roll-cast neat BCP. The clay reinforced material also strain hardens earlier and at a greater rate. The production of such parallel/parallel C−BCP nanocomposites should have dramatic impact in increasing the barrier properties of thermoplastic elastomers.

Acknowledgment. We thank Dr. R. Vaia and Dr. J. Groenewold for insightful discussions. We also thank Southern Clay Products and Dexco Polymers (especially Dr. B. Sinha for the PDI information) for supplying materials. Research support was through the Air Force sponsored DURINT project on Polymer Nanocomposites at the Massachusetts Institute of Technology under Grant F49620-01-1-0447.

References and Notes

(1) Giannelis, E. P. *Adv. Mater.* **1996**, *8*, 29−35.
(2) Manias, E.; Touny, A.; Wu, L.; Strawhecker, K.; Lu, B.; Chung, T. C. *Chem. Mater.* **2001**, *13*, 3516−3523.
(3) Kojima, Y.; Usuki, A.; Kawasumi, M.; Okada, A.; Fukushima, Y.; Kurauchi, T.; Kamigaito, O. *J. Mater. Res.* **1993**, *8*, 1185−1189.
(4) Kojima, Y.; Fukumori, K.; Usuki, A.; Okada, A.; Kurauchi, T. *J. Mater. Sci., Lett.* **1993**, *12*, 889−890.
(5) Vaia, R. A.; Price, G.; Ruth, P. N.; Nguyen, H. T.; Lichtenhan, J. *Appl. Clay Sci.* **1999**, *15*, 67−92.
(6) Lee, T. W.; Park, O. O.; Yoon, J. H.; Kim, J. J. *Adv. Mater.* **2001**, *13*, 211−213.
(7) Garces, J. M.; Moll, D. J.; Bicerano, J.; Fibiger, R.; McLeod, D. G. *Adv. Mater.* **2000**, *12*, 1835−1839.
(8) Jiang, L. Y.; Leu, C. M.; Wei, K. H. *Adv. Mater.* **2002**, *14*, 426.
(9) Laus, M.; Francescangeli, O.; Sandrolini, F. *J. Mater. Res.* **1997**, *12*, 3134−3139.
(10) Galanti, A.; Laus, M.; Fiorini, M. *Kautsch. Gummi Kunstst.* **1999**, *52*, 21−25.
(11) Silva, A. S.; Mitchell, C. A.; Tse, M. F.; Wang, H. C.; Krishnamoorti, R. *J. Chem. Phys.* **2001**, *115*, 7166−7174.
(12) Ren, J. X.; Silva, A. S.; Krishnamoorti, R. *Macromolecules* **2000**, *33*, 3739−3746.
(13) Krishnamoorti, R.; Silva, A. S.; Mitchell, C. A. *J. Chem. Phys.* **2001**, *115*, 7175−7181.
(14) Dumitru, P.; Lees, G. C.; Liauw, C. M.; Rothon, R. N. *Macromol. Symp.* **2001**, *170*, 213−220.
(15) Lim, Y. T.; Park, O. O. *Korean J. Chem. Eng.* **2001**, *18*, 21−25.
(16) Ha, Y. H.; Thomas, E. L. *Macromolecules* **2002**, *35*, 4419−4428.
(17) Vaia, R. A.; Giannelis, E. P. *Macromolecules* **1997**, *30*, 7990−7999.
(18) Vaia, R. A.; Giannelis, E. P. *Macromolecules* **1997**, *30*, 8000−8009.
(19) Balazs, A. C.; Singh, C.; Zhulina, E.; Lyatskaya, Y. *Acc. Chem. Res.* **1999**, *32*, 651−657.
(20) Balazs, A. C.; Singh, C.; Zhulina, E. *Macromolecules* **1998**, *31*, 8370−8381.
(21) Groenewold, J.; Fredrickson, G. H. *Eur. Phys. J. E* **2001**, *5*, 171−182.
(22) Fukushima, Y.; Inagaki, S. *J. Inclusion Phenom.* **1987**, *5*, 473−482.
(23) Usuki, A.; Kojima, Y.; Kawasumi, M.; Okada, A.; Fukushima, Y.; Kurauchi, T.; Kamigaito, O. *J. Mater. Res.* **1993**, *8*, 1179−1184.
(24) Beyer, F. L.; Tan, N. C. B.; Dasgupta, A.; Galvin, M. E. *Chem. Mater.* **2002**, *14*, 2983−2988.
(25) Hasegawa, R.; Aoki, Y.; Doi, M. *Macromolecules* **1996**, *29*, 6656−6662.
(26) Hasegawa, N.; Usuki, A. *Polym. Bull. (Berlin)* **2003**, *51*, 77−83.
(27) Lee, J. Y.; Park, M. S.; Yang, H. C.; Cho, K.; Kim, K. C. *Polymer* **2003**, *44*, 1705−1710.
(28) Weimer, M. W.; Chen, H.; Giannelis, E. P.; Sogah, D. Y. *J. Am. Chem. Soc.* **1999**, *121*, 1615−1616.
(29) Ueda, K.; Hirao, A.; Nakahama, S. *Macromolecules* **1990**, *23*, 939−945.
(30) Hoffmann, B.; Dietrich, C.; Thomann, R.; Friedrich, C.; Mulhaupt, R. *Macromol. Rapid Commun.* **2000**, *21*, 57−61.
(31) Sinha, B., 2004.
(32) Cohen, Y.; Albalak, R. J.; Dair, B. J.; Capel, M. S.; Thomas, E. L. *Macromolecules* **2000**, *33*, 6502−6516.
(33) Albalak, R. J.; Thomas, E. L. *J. Polym. Sci., Part B: Polym. Phys.* **1993**, *31*, 37−46.
(34) Albalak, R. J.; Thomas, E. L.; Capel, M. S. *Polymer* **1997**, *38*, 3819−3825.
(35) Hammersley, A. P. ESRF Internal Report ESRF97HA02T, 1997.
(36) Hammersley, A. P.; Svensson, S. O.; Hanfland, M.; Fitch, A. N.; Hausermann, D. *High Pressure Res.* **1996**, *14*, 235−248.
(37) Yano, K.; Usuki, A.; Okada, A. *J. Polym. Sci., Polym. Chem.* **1997**, *35*, 2289−2294.
(38) Kojima, Y.; Usuki, A.; Kawasumi, M.; Okada, A.; Kurauchi, T.; Kamigaito, O. *J. Appl. Polym. Sci.* **1993**, *49*, 1259−1264.
(39) Messersmith, P. B.; Giannelis, E. P. *J. Polym. Sci., Polym. Chem.* **1995**, *33*, 1047−1057.
(40) Ha, Y. H.; Thomas, E. L. Manuscript in preparation.
(41) Ma, M.; Vijayan, K.; Hiltner, A.; Baer, E. *J. Mater. Sci.* **1990**, *25*, 2039−2046.
(42) Allan, P.; Arridge, R. G. C.; Ehtaiatkar, F.; Folkes, M. J. *J. Phys. D* **1991**, *24*, 1381−1390.
(43) Jones, R. M. *Mechanics of Composite Materials*; McGraw-Hill: New York, 1975.
(44) Tzianetopoulou, T.; Boyce, M. C. *MRS Proc., Fall* **2003**, *788*, L9.3. Ha, Y.-H.; Kwon, Y.; Breiner, T.; Chan, E. P.; Tzianetopoulou, T.; Cohen, R. E.; Boyce, M. C.; Thomas, E. L. *Macromolecules*, in press.

MA0476792